Imaging-Based Characterization of Calcite-Filled Fractures and Porosity in Shales

Bolivia Vega, Cynthia M. Ross, and **Anthony R. Kovscek,** Stanford University

Summary

Gas- and liquid-rich shales exhibit structural and compositional features across a broad range of length scales from meters to nanometers. This laboratory characterization effort of a shale sample aids hydrocarbon resource and reserves estimation, and improves understanding of flow behavior including potential geological carbon dioxide storage. Multiscale laboratory-imaging techniques were applied to characterize pore and microfracture structure of a Barnett Shale sample including connectivity and heterogeneity. X-ray computed tomography (CT) illuminated the krypton (Kr)-accessible porosity of centimeter-sized shale cores. Transmission X-ray microscopy (TXM) imaged micrometer-sized shale samples, and high-resolution scanning electron microscopy (SEM) revealed pore, fracture, and textural features. Registration of 190 μm resolution CT images with micrometer to nanometer resolution TXM and SEM images improved physical understanding of transport through organic-rich shale. Results focus on calcite-filled fractures and the calcite/shale-matrix interface as well as the distribution of micrometer- and nanometer-scale porosity. Fractures are likely both natural and induced. For the sample studied, pore accessibility determined by CT imaging corresponds with open microfractures that cross calcite-filled fractures and adjacent shale matrix. Such observations are made with corresponding micrometer- to nanometer-scale SEM images as well as compositional data. Taken together, these data indicate that calcite-filled fractures in this core act as a barrier to flow parallel to bedding except where breached by numerous open fractures. In contrast, these filled fractures enhance vertical flow, that is, flow between laminations. A region containing porosity and organic matter (with dimensions of tens to hundreds of nanometers) determined by 3D nanocharacterization with TXM and focused ion beam/SEM at the filled-fracture/shale-matrix interface facilitates this observed gas transport along the wall of the fracture fill. Areas adjacent to calcite-filled fractures and carbonaceous laminations within the shale matrix of the study sample are most readily accessed by Kr and may therefore be more readily produced than comparatively clay-rich laminations. The numerous open fractures and sheet pores within the calcite fracture fill, as well as the inherent weakness of the porosity and organic matter at the fracture-fill/shale-matrix interface, are indicative of its susceptibility to reopening and fracturing.

Introduction

Shales and related rock types (e.g., mudstones), hereafter referred to as shales, constitute a significant component of the petroleum-reservoir geological inventory, and have been historically regarded as either source or seal rocks (Gale and Holder 2010). Once overlooked as a viable energy resource, shale plays have evolved into an important resource for the United States, in which shale natural-gas estimated production reached 10,371 Bcf in 2012 (EIA 2012). In addition, widespread consumption of fossil fuels has led to emission of greenhouse gases. One of the methods to reduce carbon dioxide (CO_2) concentration in the atmosphere is to sequester or store it in geological formations such as depleted oil reservoirs and saline aquifers (IPCC 2005). To improve economic viability and environmental quality, geological sequestration activities should be considered in conjunction with enhanced recovery (EOR) of oil and natural gas. Shales and coals are potential sites for subsurface sequestration of CO_2 because of their capability to store free and sorbed gas, presumably within their organic component (Wong et al. 2000; Nuttall et al. 2005; Jessen et al. 2008; Lin et al. 2008; Harris et al. 2008).

Shales are a mixture of ultrafine-grained components including clay, carbonate, silica, and pyrite as well as, potentially, organic matter (OM). Despite their small pore sizes, shales often present multimodal pore distributions (Akkutlu and Fathi 2011). Organic-rich shales often contain an accumulation of hydrocarbons within low-permeability matrices and adsorbed to OM. The Mississippian Barnett Shale from the Fort Worth Basin (Texas, USA) is a substantial resource with 43.43 Tcf of original gas in place (USGS 2013). This formation is mainly composed of silica- and carbonate-rich mudstones with high OM content (Loucks and Ruppel 2007). The Barnett is defined as thermogenic rock with high thermal maturity (Jarvie et al. 2007). It was deposited in a deep, predominantly dysaerobic-to-anoxic foreland marine basin during the Mississippian, in which strata were heated to temperatures between 100 and 180°C (Loucks et al. 2009). Montgomery et al. (2005) establish the uniqueness of the Barnett Shale on the basis of attributes such as its depth and overpressurization, its thermogenic origin, and complex thermal history. Natural fractures in the Barnett Shale are common, have narrow apertures ($<$0.05 mm), are typically sealed with calcite, and are present as en echelon arrays (Gale et al. 2007).

There is a general consensus that fractures are important to gas producibility. Production depends on natural- and stimulated-fracture permeability to provide transport conduits (Jarvie et al. 2007). Natural fractures are relevant for shale production because they either interact with hydraulic fractures or contribute directly to storage and permeability (Gale et al. 2007). The degree of natural-fracture development, in an otherwise low matrix permeability, is a production-controlling factor (Curtis 2002). Assessment of natural fracturing in shale plays is desirable for the prediction of prospects and for modeling the petroleum system to quantify the associated risks (Gasparrini et al. 2014).

The role of fractures on storage capacity and permeability is widely discussed. Montgomery et al. (2005) assert that natural fractures are not essential for production, and opine that, in some cases, they may reduce well performance because of their observations of opening-mode fractures sealed with calcite. Bowker (2007) adds that the Barnett's natural fractures are completely healed with carbonate cements, and they have nothing to do with productivity. Other authors (Gale et al. 2007; Gale and Holder 2008; Gale and Holder 2010; Gasparrini et al. 2014) have directed their work toward understanding the fundamental processes controlling fracture propagation in shales. They agree that after the fractures are sealed, they are no longer a pathway for fluid flow (Laubach 2003); however, they also argue that, in Barnett examples, the junction between the fracture-wall matrix and cement is weak. The dominant calcite cement grows mostly over noncarbonate grains and does not form a chemical bond between cement

This paper (SPE 1922521) was accepted for presentation at the SPE/AAPG/SEG Unconventional Resources Technology Conference, Denver, 25–27 August 2014, and revised for publication. Original manuscript received for review 23 May 2014. Revised manuscript received for review 22 October 2014. Paper peer approved 16 December 2014.

Instrument	Application
GE HiSpeed CT/I helical medical scanner	Nondestructive 3D imaging, resolution: 0.19 × 0.19 × 1 mm. 120 mA, 80 keV.
SLAC Xradia nanoXCT S100 full-field TXM 3D tomographic imaging (20- to 30-μm FOV)	Nondestructive 3D imaging, resolution: 21 × 21 × 21 nm. 7 keV.
JEOL JSM-5600LV SEM with an EDAX Sapphire Si(Li) EDS with GENESIS software (15 kV)	Low-resolution 2D images (SEI, BSE, and CL; 1,000X), mosaics and elemental maps.
FEI XL30 Sirion SEM with FEG source and EDAX Sapphire Si(Li) EDS with GENESIS software (3 to 15 kV)	Medium- to high-resolution 2D images (BSE and SEI) and elemental maps.
JEOL JXA-8230 SuperProbe with 5 dual-crystal wavelength dispersive spectrometers and automated with Advanced Microbeam hardware and PROBE-PRBSE software, JEOL EDS, xClient III Advanced Hyperspectral CL system	2D images (BSE and color CL) and compositional data.
FEI Helios NanoLab 600i DualBeam FIB/SEM (3 kV)	3D images, 4 × 4 × 36-nm resolution.
FEI Quanta 200 SEM with tungsten filament and Oxford Instruments Nordlys-F+ with 4 forescatter detectors as well as X-Max 20 mm^2 EDS. Processing performed with Aztec and Channel5 software.	2D images (BSE and EBSD) and elemental maps. EBSD data collected with 0.4-μm steps.
Rubotherm magnetic-suspension microbalance	Sorption measurements.

Table 1—Instruments and their application.

and wall rock. Sealed fractures may be prone to reactivation in shear or opening mode during hydraulic-fracture treatment (Gale et al. 2007; Gale and Holder 2010). They assert that these common narrow Barnett natural filled fractures act as planes of weakness with low tensile strength due to the lack of crystallographic continuity of the fracture growth in the wall rock (Gale et al. 2007). Bowker (2007) later concedes that the healed fractures act as zones of weakness that serve to deflect the growing induced fracture, and states that "the Barnett is not a fractured-shale play; it is a shale-that-can-be-fractured play."

Shale composition and fabric influence structure and properties such as methane sorption and brittleness. Ross and Bustin (2008, 2009) concluded that inorganic material influences pore size, porosity, and sorption of shales, as well as the natural-fracture genesis and designs for fracture stimulation. Gasparrini et al. (2014) characterized petrographically and geochemically the fracture-sealing minerals of the Barnett Shale, and described four types of fractures according to factors such as timing of compaction, burial depth, fracture mechanisms, and parent fluids. Laubach (2003) presented a thorough study of fracture diagenesis and how mineral deposits provide valuable information on the timing of the fracture-development events, as well as on the potential for these fractures to influence porosity and permeability of the fracture system. Guo et al. (2012) explored the mineralogy of the Barnett and concluded that brittleness increases with quartz, calcite, and dolomite content leading to the presence of crack-like pores in the Barnett Shale. In particular, Gale et al. (2007) and Gale and Holder (2008) measured subcritical crack index and tensile strength of Barnett Shale samples with and without calcite-sealed fractures. They found the subcritical crack index to be high, indicating that large opening-mode fractures are likely to be clustered. They found tensile strength along fractures sealed with calcite to be half that of the host rock without the fractures. In their tensile strength and bending tests study, all specimens containing calcite-filled fractures ruptured along the fracture plane, and, in extreme cases, the cement parted from both fracture walls, leaving a completely detached thin sliver (Gale and Holder 2010), whereas those samples without cemented fractures broke in different locations.

This work explores the interplay of calcite-cemented fractures and carbonates within the shale matrix with respect to gas transport through a Barnett core sample. Multiple imaging techniques of various spatial resolution form the basis of the analysis. Registration of X-ray computed-tomography (CT) images and scanning electron microscopy (SEM) images reveals details regarding the accessibility of pore space. In subsequent sections, the suite of imaging and analytical techniques is described including SEM with secondary electron (SEI), backscattered electron (BSE), total and color cathodoluminescence (CL), electron backscatter diffraction (EBSD), and energy dispersive spectroscopy (EDS) detectors as well as electron microprobe analysis (EMPA), transmission X-ray microscopy (TXM), and focused ion beam (FIB) 3D reconstruction. For methods with limited field of view (FOV), mosaics were constructed. Sorption measurements were conducted under imaging temperature and pore-pressure conditions to determine adsorption of krypton (Kr) on calcite and illite. The combined results for fracture/matrix characterization explain the distribution of gas in core-scale samples. The contribution of the calcite microstructure, the calcite/organic-material interface, and the calcite/mineral interface to transport through shale is clarified.

Methods

The experimental techniques and imaging apparatus are many and have different strengths. **Table 1** summarizes the analytical tools used. Each technique is discussed in turn. The samples used for this study come from a single Barnett core and its end trims. Samples and sample-preparation techniques are also presented.

X-Ray CT. CT scanning is a nondestructive imaging technique that provides 2D and 3D images of opaque objects. It is relatively easy to apply, offers fine spatial resolution, and is adaptable to many types of experimental procedures. X-ray imaging offers unique insight into a material's inner structure and configuration. Each element, molecule, and combination of materials, phases, and systems has X-ray attenuation (quantified as CT number) properties that allow an amount of X-rays to pass to the detectors. Density is proportional to X-ray attenuation; thus, smaller-density materials have smaller X-ray attenuation properties than larger-density materials and a smaller CT number. In a porous medium at ambient conditions, it is assumed that air fills the pore space and fracture networks. If the air is removed and replaced by a gas such as Kr that attenuates X-rays more strongly, a greater contrast between images is achieved. Details of the use of Kr to study core-scale gas shale samples are found in Vega et al. (2014).

Provided that the solid matrix does not change between measurements with one gas and the other, the difference between the images is proportional to the pore space accessed by gas. **Fig. 1a** illustrates the coreholder system used to image the Barnett core sample. A confining pressure of 300 psi is applied. The sample is dried, scanned while filled with air, vacuum evacuated, and then Kr is injected at 100 psi (689 kPa). After Kr reaches the opposite end of the core and pressure equilibrates, the sample is imaged again. Kr-filled porosity, ϕ, is quantified as

$$\phi = \frac{CT_{\text{sat}} - CT_{\text{dry}}}{CT_{\text{Fluid 1}} - CT_{\text{Fluid 2}}}, \quad \ldots\ldots\ldots\ldots\ldots\ldots (1)$$

where CT_{sat} is the CT number matrix obtained from the image of core sample saturated with Fluid 1, CT_{dry} is the CT number matrix

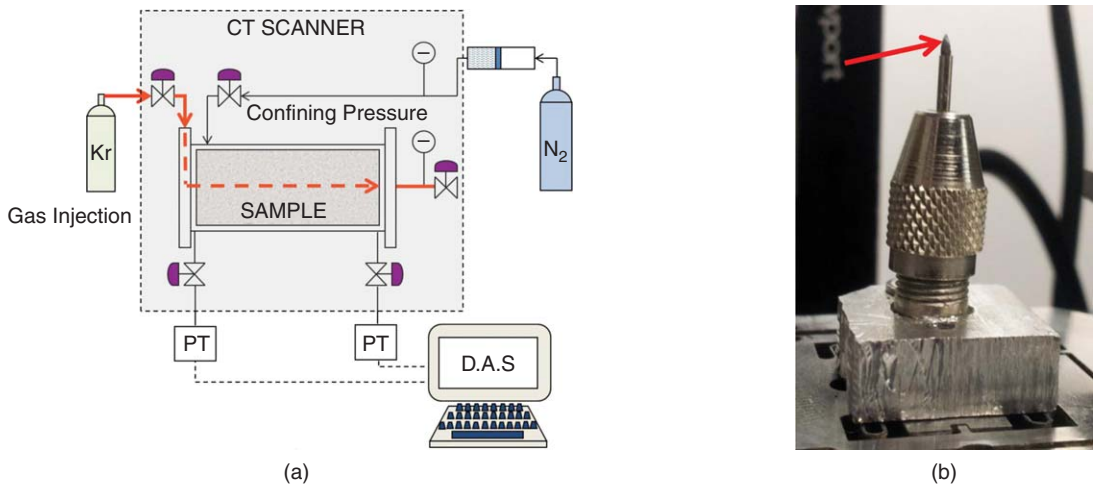

Fig. 1—(a) X-ray CT scanner imaging apparatus for shale core sample, (b) needle-mount sample setup for TXM studies. Red arrow points to FIB-prepared sample.

obtained from the image of core sample saturated with Fluid 2, $CT_{\text{Fluid 1}}$ is the CT number of Kr at experimental conditions, and $CT_{\text{Fluid 2}}$ is the CT number of air at experimental conditions. Note that if the penetrant adsorbs to pore surfaces, Eq. 1 yields an "apparent" porosity because pore fluid is not differentiated from adsorbed fluid. In this case, Eq. 1 represents the ratio of the volume of gas in place at a specific pressure upon the rock bulk volume.

The CT scanner is a GE HiSpeed CTi fifth-generation medical scanner operated in helical mode. The voxel dimension is $0.19 \times 0.19 \times 1$ mm, the tube current is 120 mA, and the energy level of the radiation used was 80 keV. The images obtained with both scanners display sufficient contrast among rock features and do not exhibit detectable positioning errors because of either energy level or positioning system.

Full-Field Transmission X-Ray Microscope (TXM). Parts of this study were conducted at the Stanford Synchrotron Radiation Laboratory's beamline 6-2c that houses an Xradia nanoXCT S100 TXM powered by a synchrotron monochromatic light source. The instrument features an array of unique capabilities that include 30-μm field of view (FOV), spatial resolution of 20 to 30 nm, high penetration (≈1 to 20 μm) for nondestructive imaging of relatively thick samples, and absorption contrast in the approximately 5- to 14-keV range (Andrews et al. 2008; Liu et al. 2011). In addition to 2D imaging with high spatial resolution, the TXM is also used for tomographic 3D imaging. This capability allows the capture of images of structures resolved to a few tens of nanometers more than an FOV of a few hundred micrometers. TXM is capable of imaging in real time and also of creating tiled-image composites, or "mosaics," that allow covering a larger area of the sample in case its size surpasses the FOV of the instrument, which varies between 30 and 40 μm. Although the mosaic images are useful in assessing larger regions, the study volume needs generally to be constrained for 3D tomography because of the time limitations that are usually imposed on experiments at synchrotron facilities.

The TXM sample holder requires the sample to be mounted vertically and perpendicular to the beam. The shale sample was glued to the top of a flat-tipped pin. The pin was then set directly on a sample holder (Fig. 1b). The X-ray energy level was 7 keV.

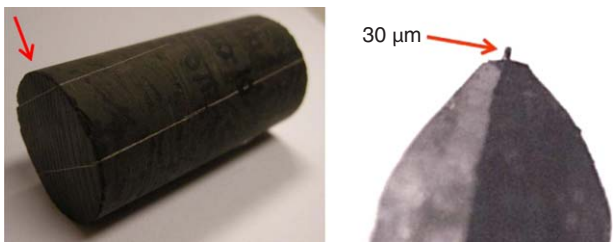

Fig. 2—(a) Barnett Shale core sample. Notice the two fractures filled with calcite along the length of the core. Arrow approximates bedding orientation. (b) FIB-prepared TXM sample containing calcite-filled-fracture/matrix interface (not visible). Sample is from material immediately adjacent to the core. This sample is also shown in Fig. 1b.

Samples. A horizontal Barnett core plug from a depth of 8620.1 ft (2627 m) within the Fort Worth Basin is the main subject (**Fig. 2a).** The 2.54×5.18-cm core has a helium (He) porosity of 5.5% and a Kr porosity of 7.8%, as measured by Aljamaan (2013), using Boyle's law, and a permeability of 5.34 μd. X-ray diffraction (XRD) compositional data (wt%) are summarized in **Table 2.** Visible on the outer surface of the core are two filled fractures that are planar and oriented roughly parallel to each other (Fig. 2a). The fractures are at a slight angle to the long axis of the core. One fracture extends the entire length of the core, progressing from one side toward the center of the core, whereas the other fracture begins at one side and angles out of the core just short of the opposite end.

For TXM imaging, sample dimension is usually one order of magnitude greater than the scale that it is being imaged. In this case, nanoscale imaging then requires a micrometer-dimensioned sample. This sample was from a trim end that was immediately adjacent to the core shown in Fig. 2a. FIB milling by means of an outside vendor shaped a 30 μm diameter shale cylinder on a shale fragment (Fig. 2b). Special care was taken in ensuring that the 30 μm diameter cylinder volume contains both shale matrix and calcite fracture fill.

A suite of samples for SEM, electron microprobe analysis (EMPA), and FIB imaging was prepared from trim ends of the core plug as well as an 8 mm thick disk sliced off the actual core sample after CT contrast imaging. Irregularly shaped pieces were embedded in cold-setting epoxy such that the resulting polished surfaces were perpendicular to bedding and filled fractures. The core disk and embedded samples were polished using incrementally finer grit (i.e., 6- and 1-μm diamond suspension), with a final polish using colloidal silica. Depending on the application, polished samples were coated with either gold or carbon. For electron backscatter diffraction (EBSD), the sample was left uncoated. After imaging was completed on one side of the disk, the other side was polished, coated, and imaged.

SEM Mosaic Construction. Overlapping SEM backscattered electron (BSE) images at 75X were collected and compiled using Adobe Photoshop CS5.1 for the entire core face on both sides of

	Feldspars		Carbonates		Clays		Sulfates	Sulfides	
Quartz	K-Feldspar	Plagioclase	Calcite	Fe Dolomite	Illite	Mixed Layer Illite/Smectite	Barite, Gypsum, Anhydrite	Pyrite	TOC
45.0	0.0	5.8	7.6	2.8	19.0	6.3	0.0	1.7	12.0

Table 2—XRD composition and total organic carbon (TOC) content of Barnett Shale sample (wt%) with a calculated grain density of 2.678 g/cm^3.

an 8 mm thick slice. The slice was sawn from one end of the core and polished. Pixel resolution of 2.63 μm was obtained, and the resulting mosaic was compared with CT images and the corresponding cross-sectional Kr porosity map. At this resolution, one voxel face in the CT data is equivalent to a 72×72 pixel area in the mosaics. The first mosaic corresponds to the front face of the core (Fig. 2a). The second mosaic is a planar representation of a parallel slice 8 mm from the front face of the core. While the second mosaic was imaged, the failing filament generated photomicrographs with uneven illumination. Although the resulting mosaic was useful in locating fractures and carbonate-rich areas, measuring fracture apertures, and comparing with CT images, it is not suitable for publication. Further mosaics may be constructed for other slices of the core after the experiments are completed. Higher-resolution mosaics (200 and 250X) were constructed covering the length of the filled fractures of the two core faces. Before the disk was sliced from the study core, a 75X mosaic was constructed on a sample collected from material immediately adjacent to the core. Much of the nanoscale characterization was conducted on this trim end sample.

Fracture-Fill Characterization Methods. Examination of the matrix and fracture fill used SEMs with SEI, BSE, CL, EBSD, and EDS detectors. In addition, color CL and BSE images as well as compositional data were collected by means of EMPA. The 3D nanocharacterization was accomplished with FIB/SEM with 36-nm slice spacing. To counter limited FOV, overlapping images were collected and compiled into mosaics providing higher-resolution images covering a more representative area. Image magnifications range from 35 to 100,000X with a few images as high as 350,000 and 500,000X.

Results

Results are presented from the core scale and then to subsequently finer length scales. Implications of the results are also drawn out in this section to obtain a comprehensive presentation.

3D Accessible Porosity. The resulting 3D krypton (Kr) porosity map and orthogonal slices for the Barnett core sample are shown in **Fig. 3.** Although microporosity and microfractures are present in the sample, these unresolved components are included in the composite porosity measured for each voxel (size $0.19 \times 0.19 \times 1$ mm; Eq. 1). Red shading indicates an apparent porosity of 45% or greater, whereas black is 0 to 4%. The images reveal beds dipping from the front to the opposite end along with regions that correspond to the filled fractures apparent in Fig. 2 and other heterogeneities (e.g., high-density spheres of pyrite). Average calculated computed-tomography (CT) porosity for the sample is 7.5%, comparable to the 7.8% value measured by Aljamaan (2013) using Boyle's law and Kr. Also of note are regions with apparent-porosity values as high as 50% (shown in red, Fig. 3). High localized porosity values are found adjacent to cement-filled fractures compared with the rest of the core. In the literature, localized porosity values as high as 50%, typically associated with organic matter, were reported in shales (Passey et al. 2010). Similarly, Loucks et al. (2009) measured localized nanoporosity values of 5 to 30% in Barnett samples. These localized high porosity values, however, were obtained from nanoscale images rather than micrometer-scale CT images. The large apparent porosities and their distribution within the 3D porosity map (Fig. 3) serve as the motivation for an in-depth characterization of this sample.

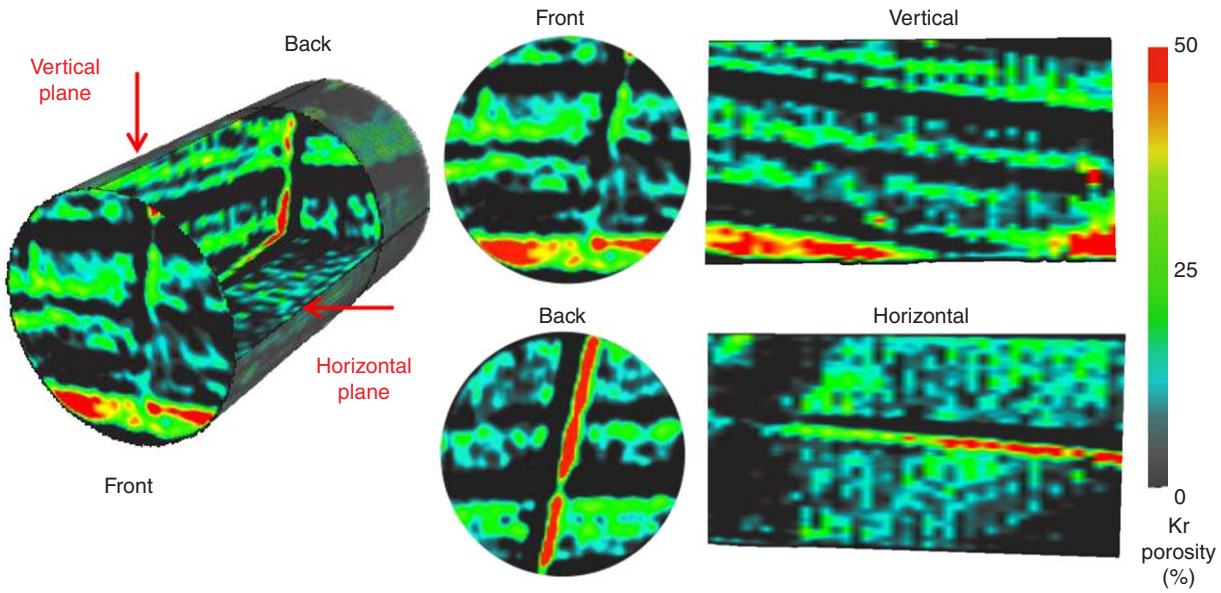

Fig. 3—The 3D Kr porosity map showing core ends and horizontal and vertical longitudinal slices under 200 psi (1379 kPa) net effective stress. Bedding surfaces dip down from the front to the back of the core. Image diameter is 2.32 cm. Arrows indicate relative orientation of planar slices.

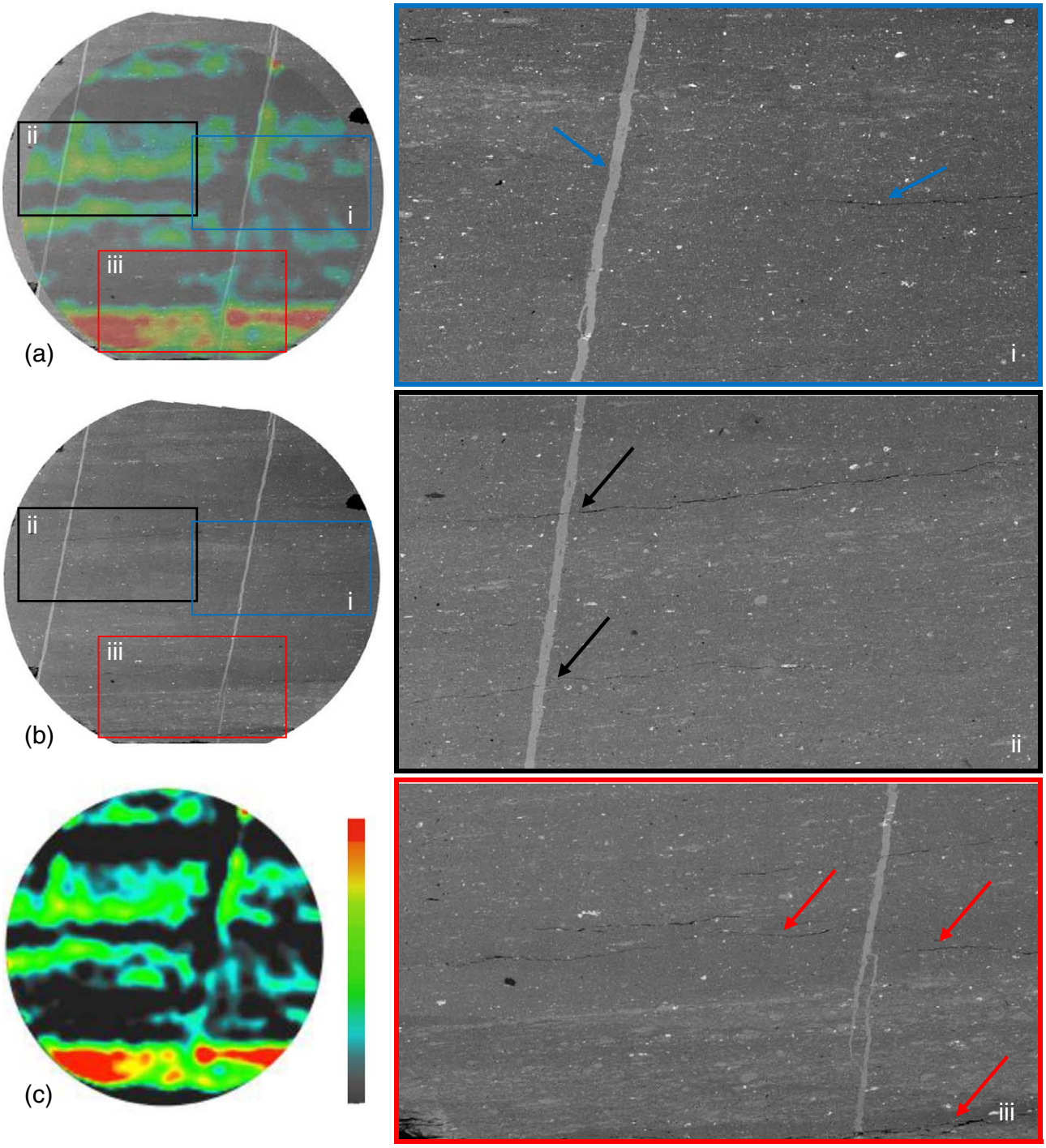

Fig. 4—Alignment of SEM BSE mosaic with overlain Kr porosity map (a), SEM BSE mosaic collected at 75X (b), and corresponding CT porosity volume slice (c). Magnified regions of interest are identified by Roman numerals (i, ii, and iii) and border color (right). Mosaic has a diameter of 2.54 cm. Calcite is a medium-gray color occurring as fracture fill and within the matrix. White areas are mostly pyrite and celestite. The apparent-porosity color map is slightly smaller to remove edge artifacts.

SEM Mosaic. Core-sized SEM backscattered electron (BSE) mosaics with a pixel resolution of 2.63 μm were aligned with corresponding Kr porosity and raw CT data slices (not shown) with a voxel face resolution of 190 μm **(Fig. 4).** After alignment, each voxel is represented by a 72×72 grid of pixels, allowing interpretation of the components contributing to the average Kr porosity and CT number per voxel. Comparisons reveal that high apparent porosity regions (40 to 50%; orange to red) correspond to carbonate-rich laminations with localized effects associated with the calcite-filled fractures (Figs. 3 and 4). The calcite-rich high-porosity lamina (15 to 50%, green to red) at the bottom of the core dips downward to the center of the core (Fig. 3, front and vertical).

Other large apparent-porosity regions are associated with pyrite and the back half of the central filled fracture (Fig. 3, horizontal, back, and lower right of vertical slice). This portion of the fracture fill may have reopened, but this could not be confirmed. A small high-porosity (red) spot at the top of front slice (Figs. 3 and 4), coincides with the filled fracture and the region surrounding it. The lamination at this location is carbonate-rich, and a longitudinal open fracture visible at 200X extends along the central portion of the calcite fracture fill. Regions with 20 to 35% apparent porosity (green) occur in carbonate-rich layers, whereas regions with 0 to 8% apparent porosity (black to dark blue) are clay dominated (Figs. 3 and 4). Calcite-filled fractures are

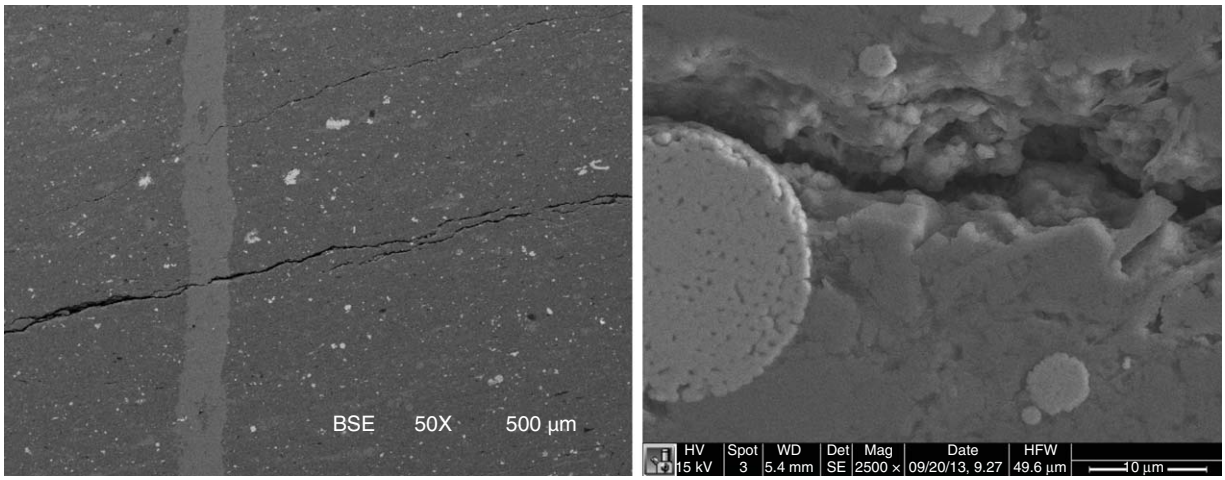

(a) (b)

Fig. 5—Open fractures oriented with bedding and crossing calcite-filled fractures in Barnett sample at 50X (a) and 2,500X (b). Inner aperture size of the fractures is 1.4 to 1.7 µm. The 2,500X image is outside the field of view of the 50X image.

oriented 75 to 80° from bedding, similar to the description of Gale et al. (2007) for Barnett cores.

Open fractures are visible subparallel to bedding in the mosaic [Fig. 4(i, ii, and iii)]. These open fractures cross calcite-filled fractures and have inner aperture diameters of 1.4 to 1.7 µm **(Fig. 5).** In most cases in which these open fractures intersect the calcite-filled fracture, apparent porosity is similar on both sides of the filled fractures. In Fig. 4(ii), the lower arrow points to such a region in which porosities are 15 to 35% on both sides of the filled fracture. In contrast, there are no visible open fractures crossing the filled fracture in the region marked by the right-facing arrow [Fig. 4(i)]; apparent-porosity values are 0 to 8% to the left of the fracture fill and 15 to 35% to the right of the fracture fill. In this case, the filled fracture is acting as a barrier diverting Kr gas along the fracture-fill/matrix interface. This effect is also observed near the upper arrow in Fig. 4(ii). Most of the open fractures occur within the relatively clay-rich laminations in close proximity to carbonate-rich layers (Fig. 4, left-facing arrows). Apparent-porosity values around open fractures are not uniform, with increased values in carbonate-rich layers; a good example of this corresponds to the region marked by the upper arrow in Fig. 4(ii). Kr gas in this open fracture preferentially entered the underlying carbonate-rich region. Example SEM BSE images, as well as the elemental composition of these two regions, are shown in **Fig. 6.** Overall, the distribution of Kr in the Barnett core corresponds to the presence of both open fractures and matrix. In addition, cemented fractures act as barriers to horizontal flow, unless breached by the numerous open fractures, and enhance vertical connectivity between beds along the fracture-fill/matrix interface. Based on the two mosaics and their 8-mm spacing, the enhanced gas transport along the interface is not caused by a reopening of the fracture. The overlay of the other SEM mosaic to its equivalent Kr porosity map reveals similar distributions of Kr, depending on proximity to both open and filled fractures as well as matrix composition. There were fractures observed in low-porosity (0 to 8%) regions. It is not known if these few fractures were induced after CT imaging either during subsequent experiments or while sawing the 8-mm disk from the core.

One aspect to consider is that the open fractures were probably narrower during Kr penetration because the core was imaged under an effective stress of 200 psi (1379 kPa), whereas the SEM samples were not subject to confining stress. This role of effective

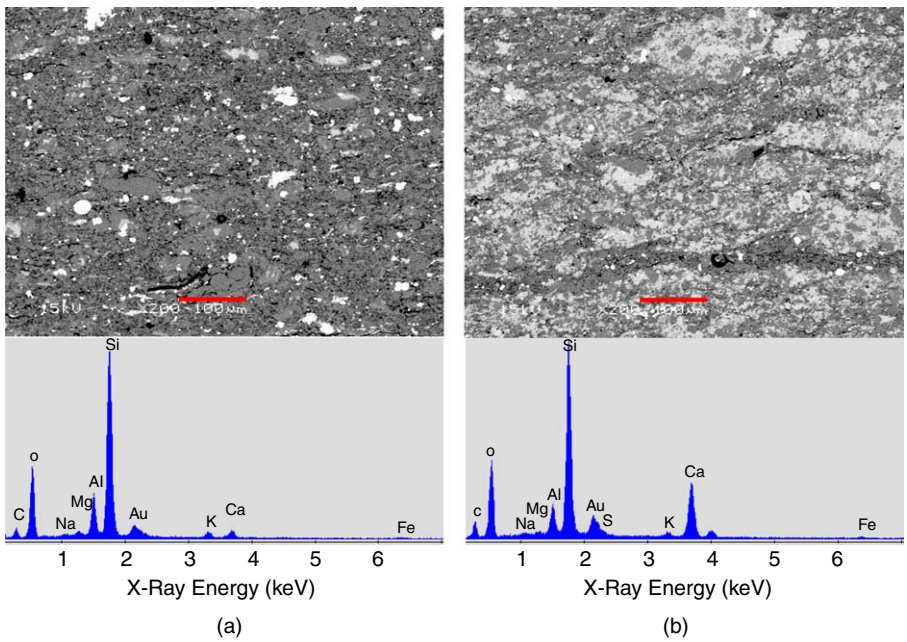

(a) (b)

Fig. 6—SEM BSE images and EDS spectra for clay-rich (a) and carbonate-rich (b) matrix areas. Scale bars (red) are 100 µm.

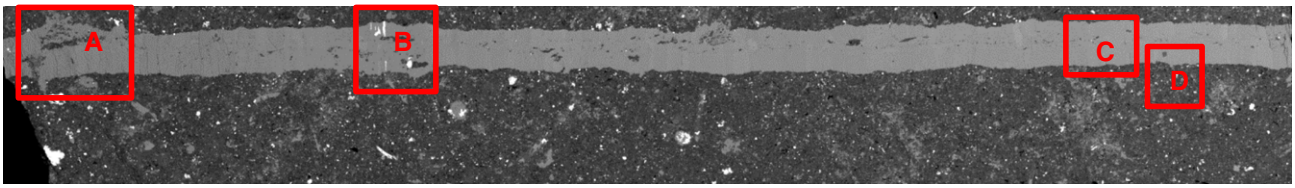

Fig. 7—SEM BSE mosaic collected at 75X showing the locations of many images and data included in this paper. The calcite-filled fracture width is 240 to 325 μm; the mosaic covers a length of 8 mm. Highlighted locations are referenced in subsequent images. This sample is from material immediately adjacent to the core.

stress is presumably more pronounced under reservoir conditions. Euhedral crystals with diameters of 1.7 to 2.5 μm can be seen within the open fractures; however, similar-sized particles also occur within the matrix as viewed on the polished surface. In the future, the core will be pulled apart to examine the fracture faces and compare them to broken surfaces of the matrix. Similar open fractures parallel to bedding were observed by other authors who attribute them to various causes such as drilling, core handling, unloading, and catagenesis (e.g., Lash and Engelder 2005; Tran et al. 2010; Josh et al. 2012). The provenance of such fractures is not the focus of this project; rather, their influence on gas accessibility is important whether these open fractures occur naturally or serve as induced proxies for hydraulic fractures.

Fracture-Fill Characterization. The fracture fill is predominantly calcite with lesser amounts of dolomite, quartz, albite, sulfates (in this case, celestite), and sulfides (pyrite). Fracture-fill compositions can be deduced within SEM BSE images in which the relative brightness correlates with the average atomic number **(Figs. 7 and 8a).** Dense minerals such as pyrite are white, whereas silicates (e.g., clays and quartz) are dark gray. The relationship between gray-scale values and elemental composition is determined with EDS measurements made at known points within the image. Another method is to use the EDS system to construct maps of selected elements (Fig. 8b). In this false-color composite elemental map, the distribution of silicon (Si—red), calcium (Ca—aqua), magnesium (Mg—green), sulfur (S—yellow), and phosphorus (P—blue) is shown. The shale matrix and some fracture-filling cements shown in red are silicates (clay, quartz, and albite), whereas the fracture fill is predominantly carbonates (calcite and dolomite, aqua and green, respectively). Authigenic quartz and albite are typically found at the matrix interface. In this particular image, the yellow sulfur-bearing regions are sulfides (pyrite). Sphalerite, a zinc sulfide, occurs in other samples from the same well and may be present, but not measured, in this sample. In other regions, yellow corresponds to celestite, a strontium-rich sulfate. Initially, celestite was misidentified as barite, because the Sr L$\propto$peak (1.806 kV) overlaps the Si K$\propto$peak (1.739 kV; Katagami 2007), and it was automatically mislabeled as Si (by all EDS systems), giving the impression of a mixed-mineralogy signal. Incorrectly identified peaks were manually corrected. In this sample, initial electron microprobe analysis (EMPA) measurements reveal a sulfate composition of ($Ba_{0–30}$, $Sr_{70–100}$) SO_4. Blue areas are small particles of apatite (calcium phosphate). Other elements mapped and not shown include aluminum (Al), barium (Ba), carbon (C), iron (Fe), potassium (K), nitrogen (N), sodium (Na), oxygen (O), and strontium (Sr) (Fig. 8b).

Significant variability is observed [via total cathodoluminescence (CL)] in the calcite fracture fill in which orderly bands are oriented from the fracture wall inward with a patchy, less-orderly region in the center of the fracture. These features are more complicated in regions containing isolated (at least in two dimensions) matrix remnants (Fig. 9c) corresponding to fracture-reactivation features and crack-seal textures, as described by Gale et al. (2007). For this figure, a CL detector that measures total luminescence was used. Carbonate minerals are problematic in that their luminescence persists (phosphorescence) causing streaking and blurring, as described by Reed and Milliken (2003). Instead of using filters, phosphorescence effects were reduced by orienting the calcite-filled fracture perpendicular to the electron-beam path. The EMPA-based color CL detector collects wavelength spectra, enabling select portions of the spectra to be displayed (not shown). In this manner, the ultraviolet-to-violet portion of the spectrum arising from carbonate

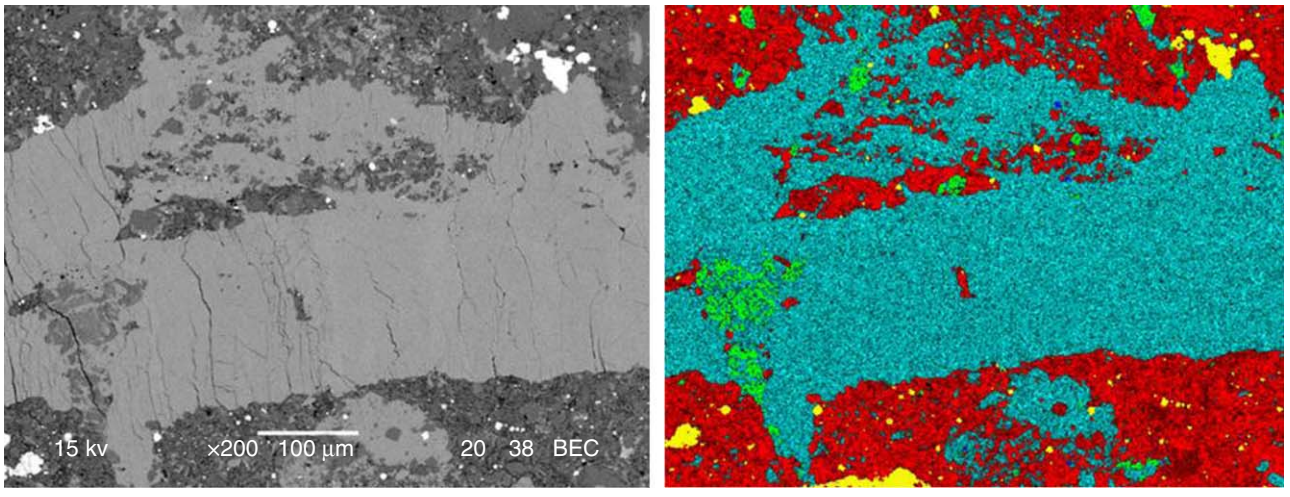

Fig. 8—(a) SEM BSE image and (b) corresponding EDS composite elemental map. [red—Si (quartz, clay, feldspars); aqua—Ca (calcite); green—Mg (dolomite); yellow—S (sulfide–pyrite, sulfate–celestite not shown); and blue—P (Ca-phosphate)]. Elements mapped and not shown—Al, Ba, C, Fe, K, O, Na, N, and Sr. Induced fractures are abundant in this area as it is at the edge of this sample (Location A in Fig. 7).

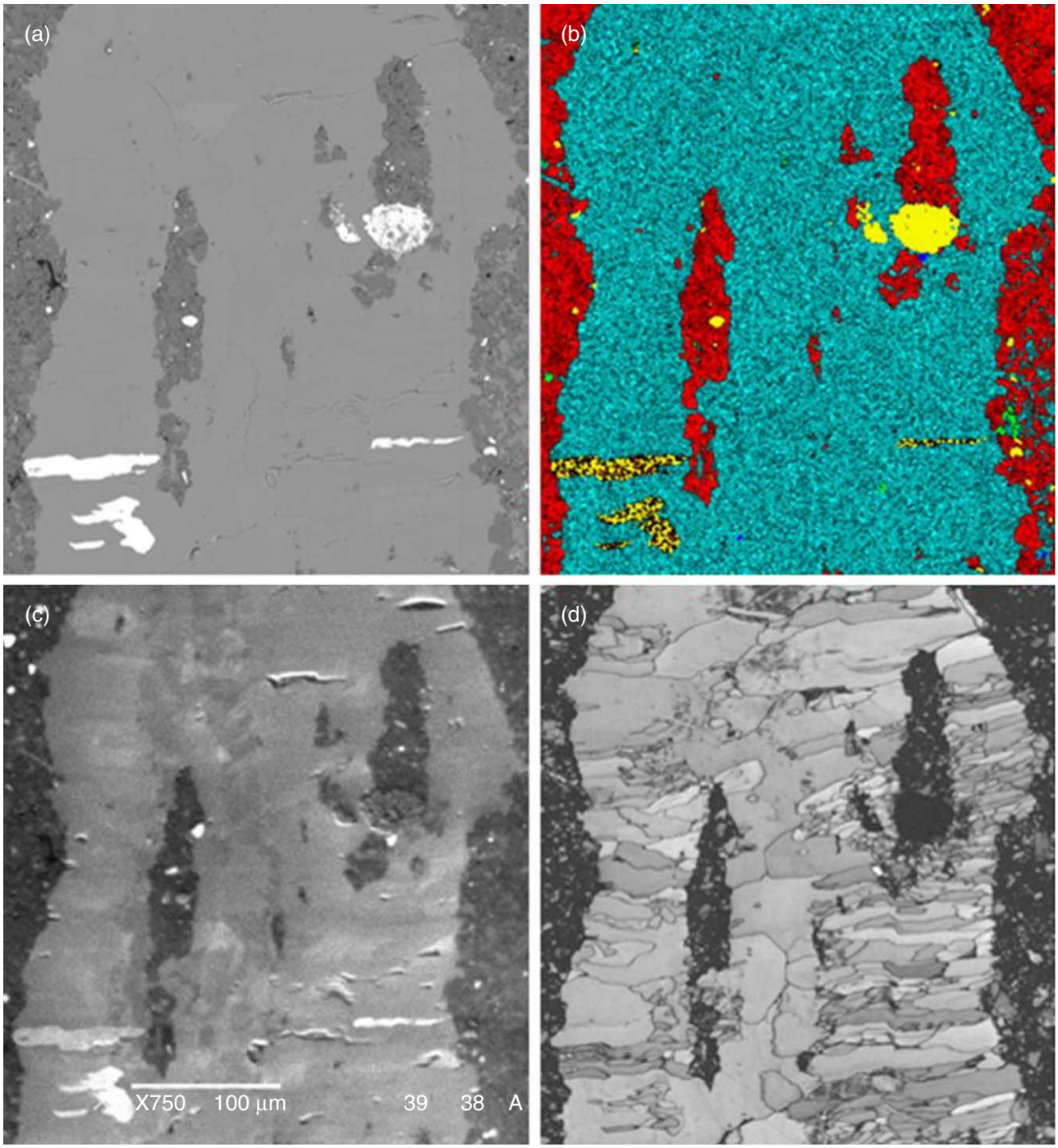

Fig. 9—Corresponding SEM images of calcite fracture fill: BSE (a), EDS composite elemental map (b), total CL (c), and EBSD (d). Color key for EDS map: red—Si (quartz, clay, feldspar); aqua—Ca (calcite); green—Mg (dolomite); yellow—S (sulfide–pyrite, sulfate–celestite); and blue—P (Ca-phosphate). Yellow and black mottled regions are celestite. (Location B in Fig. 7).

luminescence is enhanced, and the red-orange portion attributed to phosphorescence is either minimized or removed. Fracture-filling calcite exhibits similar textures with both CL imaging systems and all encountered fracture widths (100 to 325 µm). For reference, corresponding SEM SEI and EDS composite elemental maps are presented in **Figs. 9a and 9b.**

Crystal orientation of calcite within the fracture fill via EBSD provides a different view compared with total CL (Fig. 9c and 9d). In the EBSD image (Fig. 9d), different crystal orientations are assigned different grayscale values. Care was taken to better discern the patchy texture in the filled-fracture center by selecting a small step size (0.4 µm). The blocky patches apparent in the total and color CL images were expected to exhibit small, randomly oriented crystals in the EBSD images, and this seems not to be the case at this resolution. In this example, the filled fracture formed under extensional or opening conditions in several stages. Toward the top of the image, calcite grew in continuity across most of the fracture similar to that described by Papazis (2005). Where matrix remnants occur, crystal sizes are smaller.

SEM analysis of the fracture fill indicates the presence of sheet pores and possible micropores within the fill **(Fig. 10).** Sheet pores, in this case, include intercrystalline pores that are naturally occurring as well as similarly sized and somewhat larger cracks that may be natural, induced, or both. Intercrystalline sheet pores occur between calcite crystals as identified using CL imaging and shown in **Fig. 11.** Using visual estimation, intercrystalline pores are mostly oriented across the width of the fracture except in the

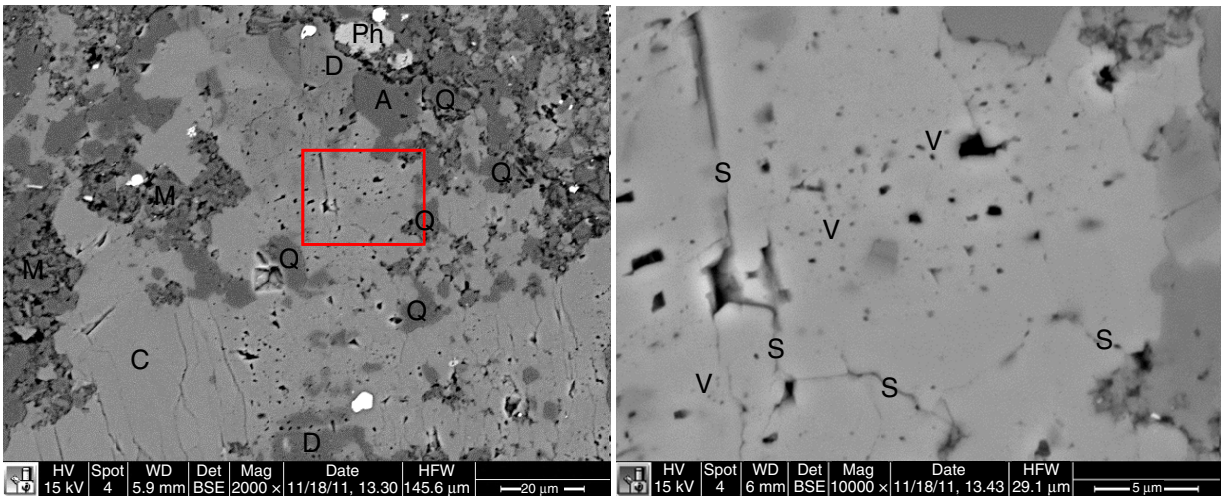

(a) (b)

Fig. 10—SEM BSE images of fracture-fill margin at (a) 2,000 and (b) 10,000X. Location of higher-magnification image (b) shown within red box (a). Sheet pores and micropores (including vacuoles) are visible. Minerals are labeled: A—albite, C—calcite, D—dolomite, Q—quartz, M—matrix, and Ph—apatite. Porosity is labeled: V—vacuoles and micropores, and S—sheet pores including induced cracks. (Location A in Fig. 7. Upper-right quadrant in Fig. 8).

patchy region toward the center of the filled fracture similar to the crystal boundary orientations within the EBSD image (Fig. 9d). Examples of induced cracks are visible in Figs. 8a and 10a. These cracks are much smaller than the open fractures shown in Fig. 5. The frequency and aperture size of these cracks increase approaching the edge of the sample, which in this case is at the left side of the image (Fig. 8a). Small cracks included with the sheet pores are largely oriented across the width of the fracture. Unlike the intercrystalline pores, these cracks are not confined to either crystal boundaries or obvious cleavage planes. Compared to the larger open fractures with large Kr porosities on both sides of filled fractures, these sheet pores, evidently, do not contribute significantly to flow across filled fractures, as shown in Fig. 4.

Micropores occur between two minerals within the fracture fill, along cleavage planes, and are most abundant in localized regions with both calcite and dolomite cements, such as the region in Fig. 10b. Micropores are most likely vacuolized calcite. Localized porosity including vacuoles, as determined with image segmentation on 2D SEM BSE images at 10,000X with 45-nm resolution, is as high as 5% in such regions. Much of the apparent microporosity, but not all, is likely isolated, consistent with the filled fractures acting as barriers to horizontal flow unless breached.

3D Nanocharacterization Transmission X-Ray Microscopy (TXM) and Focused Ion Beam/SEM (FIB/SEM). Fig. 12a is compiled from a total of 2,000 full-field projection radiographs that were collected at evenly spaced 2° intervals over a total sample rotation interval of [−90° 88°], with each radiograph exposed for 1.0 second. A 27.63 nm pixel size was obtained with a 2D field of view of 56.6 × 28.3 µm. Reference images were periodically recorded to account for changes in flux and small beam instabilities. Darker shading indicates lower density, and light shading indicates greater density. Fracture-filling calcite (red arrow) is observed on the left side of the sample, measuring approximately 6 µm in width at the top of the sample. Semispherical framboidal pyrite (blue arrows) is observed to the right of the sample. Fig. 12b shows the segmentation of some microstructures: calcite (in red), pyrite (in blue), some disconnected organic matter (OM, in yellow and aqua), and, tentatively identified, celestite (in green). Mineral and other identifications are inferred on the basis of relative density obtained from X-ray attenuation, segmentation, and morphology. An ideal way to identify components is to register TXM images with compositional maps derived with FIB/SEM serial slices; however, the FIB milling process is destructive, and we wish to use our fracture-fill/matrix interface samples for further TXM studies. Accordingly, similar, but not identical, fracture-fill/matrix interfaces are imaged with FIB/SEM for comparison.

Fig. 13 focuses on the features associated with the calcite-fracture-fill/host-rock interface. At the junction of these two materials, are dark (low-density) high-continuity pathways or microgaps consisting of OM, porosity, or both. A subsample of these low-density pathways was selected and measured on planes X–Z and

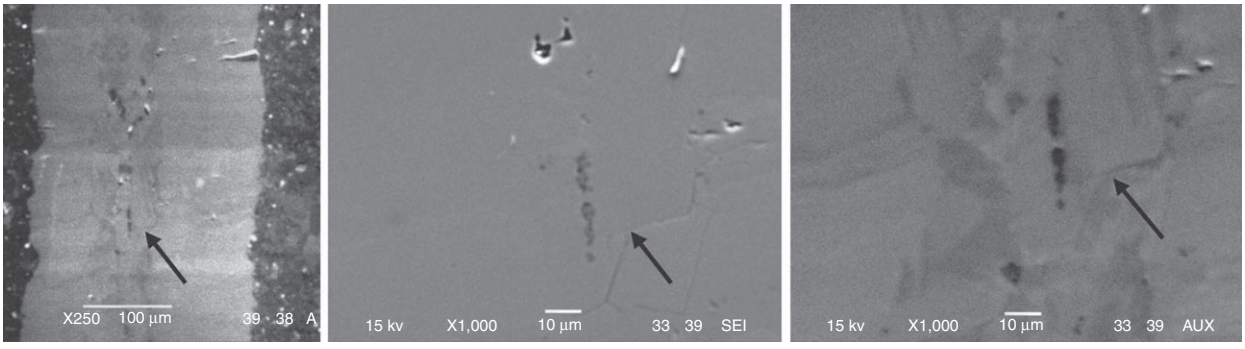

(a) (b) (c)

Fig. 11—SEM SEI image at 1,000X (b) and SEM total CL images at 250X (a) and 1,000X (c) showing sheet pores and zonation within calcite fracture-fill. Arrows point to the same location (Location C in Fig. 7).

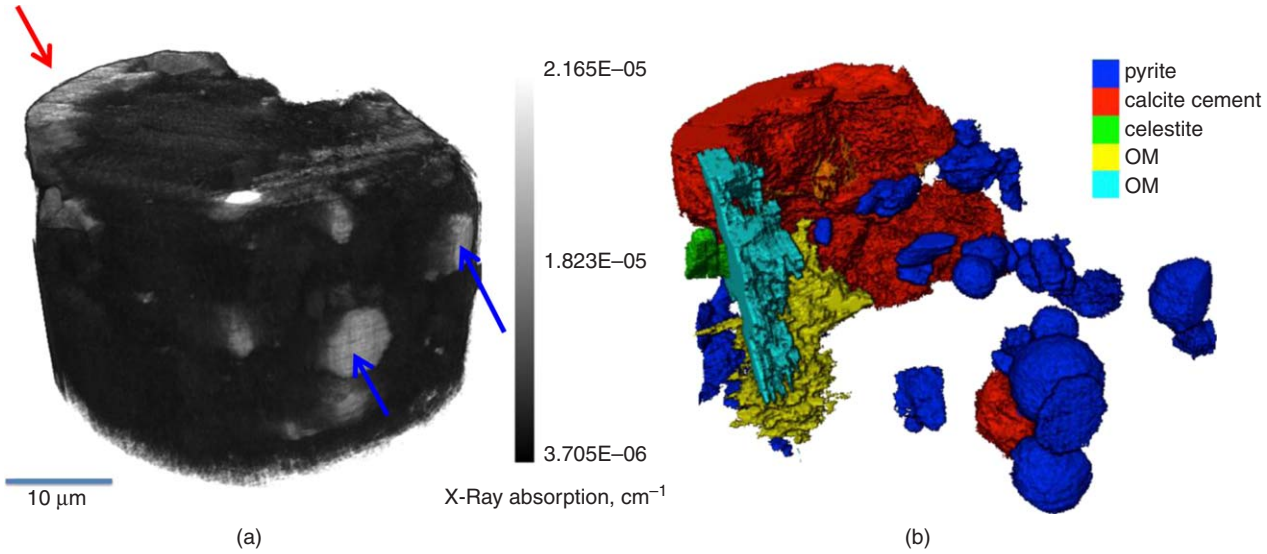

Fig. 12—(a) TXM tomogram reconstruction of Barnett Shale sample. The sample contains fracture-filling calcite cement (red arrow); pyrite framboids are also visible (blue arrows). Dark shading corresponds to low-density regions, whereas light shading indicates higher density components. (b) Segmentation of sample microstructures showing calcite (red), pyrite (blue), probable celestite (green), and two unconnected volumes of organic matter (yellow and light blue).

Y–Z, and their images are shown in Fig. 13. The measured width of the observed gaps in the calcite-fill/shale interface consistently trend between 77 and 140 nm.

Fig. 14 shows a representative portion of the gaps measured at the calcite-fracture-fill/shale interface, illustrating the distribution of these features over the junction of the fracture fill and shale matrix. Due to limitations of working at such high resolution on a large sample volume (1,200 *X–Z* planar slices), a subvolume of the sample was selected and searched for the presence of these gaps similar to those shown in Fig. 13. Gaps were found in each area scrutinized (shown in red). Gaps below the resolution of the system were not clearly discernible. The distribution of the measured gaps (in red) shows a dispersed set of small gaps that extend across the interface, suggesting the presence of a semicontinuous low-density volume between the two materials. These irregular surfaces may serve as weakness planes between the matrix and fracture fill, consistent with the observations of Gale et al. (2007), Gale and Holder (2008), Gale and Holder (2010), and Gasparrini et al. (2014). The presence of these micropathways explains the movement of Kr gas along the fracture-fill/matrix interface, as observed in Fig. 4, and may be a significant pathway for gas transport at this location.

Examination of the FIB representation of the shale-matrix/fracture-fill interface in **Fig. 15** reveals the presence of even

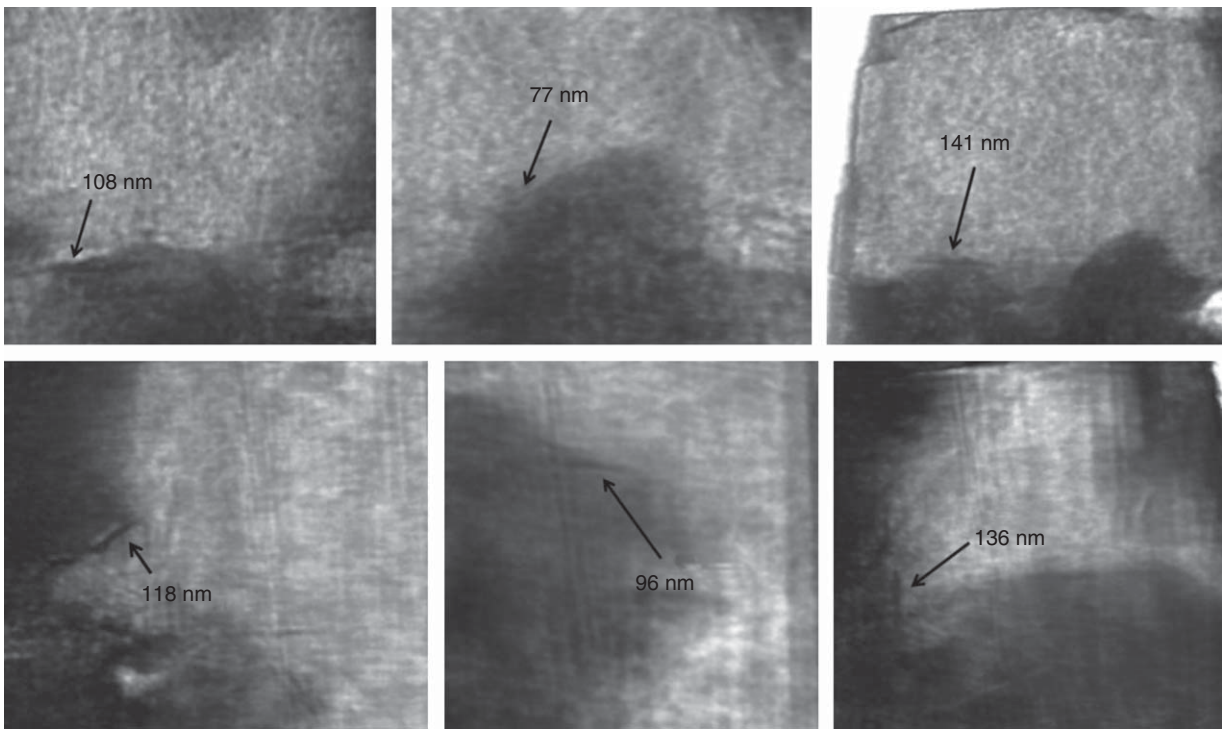

Fig. 13—Selection of cross-section images of *X–Z* and *Y–Z* planes from the volume in Fig. 12a that illustrate the presence of low-density regions (dark) between shale matrix and fracture-filling calcite cement (light). The average microgap width for this selection is 113 nm.

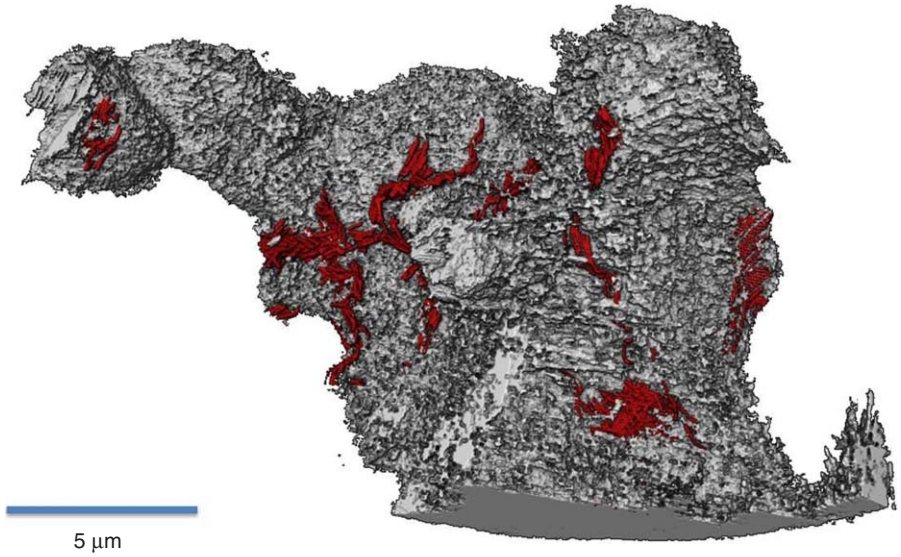

Fig. 14—Calcite-cement segmented volume (in gray) revealing topography of the calcite fracture fill with a subsample of the low-density microgaps measured at the interface with shale matrix (in red). Interface regions between the red areas contain gaps that were not measured. The presence of these microgaps suggests an inherent weakness between filled fractures and the surrounding shale matrix.

smaller voids, ranging in size from 38 to 46 nm, between the calcite and matrix components. Also observed are larger gaps (100-plus nm) filled with OM. Measured 2D porosity in OM ranges from 0 to 11.5% (SEM SEI 100,000X with 1.92-nm resolution). The larger gaps filled with OM are most likely some of the 40- to 140-nm-sized semicontinuous pathways measured with TXM imaging. Open and OM-filled spaces between calcite fracture fill and shale matrix serve as gas conduits along the fracture face, as shown in Fig. 4, and contribute to the high Kr porosity values adjacent to the low-porosity fracture fill.

Adsorption. Aljamaan (2013) measured the apparent Kr porosity of this shale sample as 7.8% using Boyle's law, whereas the He porosity was 5.5%. The average X-ray CT porosity with Kr was 7.5%, establishing consistency across these two very different measurement techniques. The greater apparent porosity to Kr as compared with He suggests adsorption of Kr to some shale components. Adsorption measurements of illite and calcium carbonate standards reveal that Kr adsorbs to calcite (0.000732 ± 0.000003 g/g) and illite (0.00225 ± 0.00002 g/g) under CT imaging conditions with a pore pressure of 100 psi (689 kPa) at room temperature (Wang 2014). The range of error given for each measurement is the standard deviation. Detailed information on the methods and inherent errors for these adsorption measurements are found elsewhere (Ottinger et al. 2006; Wang 2014). The Kr adsorption on solid surfaces is reported by a variety of authors (Beebe et al. 1945; Klington and Holmes 1953; Roberts 1960; Lockey 1960; Gregg and Sing 1982), and our measurements appear to be consistent with the literature.

OM has much greater adsorptive capacity for CO_2 and CH_4 compared to clays. We expect that this trend holds true with Kr. OM along the fracture-fill/shale interface is also present in the carbonate- and clay-rich areas of the matrix. Such OM adsorbs Kr and rationalizes the difference between He and Kr porosity. In addition, the low storage capacity (0 to 4%) in the clay-rich volumes shown in Figs. 3 and 4 suggests that even though illite and its neighboring OM are capable of adsorbing Kr, the clay-rich areas of the sample have unfavorable transport properties that make them inaccessible to Kr under experimental conditions. The tendency of Kr to store in the carbonate-rich areas suggests, in turn, that those areas have more-favorable storage and transport

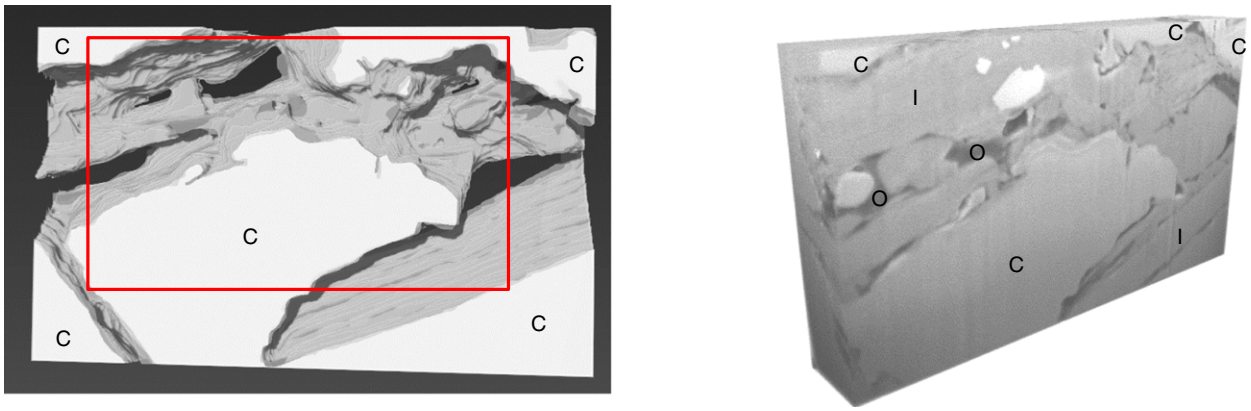

(a) (b)

Fig. 15—3D reconstruction of FIB images starting in the shale matrix and milling progressively into the wall of the adjacent calcite-filled fracture showing calcite topography (a) and subset volume (a result of charging issues) with all components (b). Components are labeled: C—calcite, I—illite, and O—OM. Region is 1,000 nm deep, with a pixel size of 4 nm and slice spacing of 36 nm (Location D in Fig. 7).

properties. At 100 psi (689 kPa) and 73°F, CH_4 does not adsorb measurably to calcite, but it does adsorb to illite (0.00093 ± 0.00001 g/g) and OM. Under subsurface conditions, the more-accessible calcite-bearing regions may contribute substantially to gas transport.

Discussion

The 2D- and 3D-imaging techniques of different resolution were applied to a Barnett Shale sample containing two visible calcite-filled fractures. Our observations and conclusions apply to this as-received core sample and its trim ends. At the mesoscale, medium- to high-porosity areas correspond to regions adjacent to calcite-filled fractures as well as to the carbonate-rich laminations of the shale (Fig. 4). Due to the millimeter-scale resolution of the computed-tomography (CT) images, contributions from features smaller than the voxel size are averaged; therefore, imaging methods of greater resolution were applied to the sample for further investigation. In a side-by-side comparison of two krypton (Kr) porosity slices and corresponding SEM mosaics, it was possible to correlate enhanced-porosity areas (5 to 50%) to structural features such as open fractures normal to the calcite fracture fill and parallel to the bedding as well as carbonate-rich laminations.

In the closer look provided by SEM-based imaging and compositional methods, various Kr porosity-enhancing features combine to make the regions adjacent to the cemented fractures and the carbonate-rich laminations more suitable for gas transport and storage. The features identified by our imaging studies include: (i) open fractures parallel to laminations and cutting across the calcite cement (Figs. 4 and 5); (ii) sheet pores and induced fractures that cross the width of the calcite fill (Fig. 8a); (iii) induced fractures that occur near the surface of the core and propagate down the central axis of the calcite cement along crystal boundaries (Fig. 9a); (iv) localized porosity within the calcite fill (Figs. 10 and 11); and (v) multiple low-density pathways at the calcite-cement/shale-matrix interface (Figs. 13 and 14). In addition to porosity, these pathways contain organic matter (OM) with inherent porosity and adsorption capacity (Fig. 15). They facilitate gas transport between laminations as evidenced by the Kr distribution within the matrix along the interface with the filled fracture (Fig. 4). The low-density region at the fracture-fill/rock-fabric interface explains, in part, the weak bond between fracture fill and shale matrix and the susceptibility of this interface region to fail. These results indicate that the Barnett sample contains a network of fractures, pathways, OM, and other components that synergistically create the transport and storage conditions observed in Fig. 3. Weak cohesion between the calcite cement and the shale fabric may be a main factor that facilitates the existence of this network, and also provides enhanced access for the gas to be adsorbed on receptive surfaces.

The fluid substitution technique used to obtain core-scale images provides qualitative and spatial information of the volumes that gas occupies. Verification with SEM imaging found that zones with large apparent porosities are carbonate-rich with some clay as well as microgaps partially filled with porous OM. We are working actively on applying the fluid substitution technique developed for core-scale to nanoscale imaging with transmission X-ray microscopy (TXM) (Vega et al. 2013). The much greater spatial resolution of TXM permits improved differentiation of pore-scale features relevant to gas storage and transport.

Conclusion

Registration of X-ray computed-tomography images using scanning electron microscopy provided a powerful means of probing and interpreting gas-flow paths through a shale sample. Generally, permeable pathways in this sample correlate, to a considerable extent, with the presence of calcite. Additional imaging and measurement techniques provided the distribution of mineralogy, measurement of open (either natural or induced) fracture dimensions, and crystallographic orientation of calcite, among other parameters.

Our main findings follow.

- Fractures filled with calcite serve as barriers to horizontal flow only if fracture-fill is continuous. Calcite-filled fractures were breached by numerous open fractures normal to fracture orientation, thereby providing conduits for gas flow.
- The porosity and organic matter filled (low-density) region immediately adjacent to fractures cemented with calcite act as conduits enhancing vertical flow between laminations.
- The interface between the fracture fill and matrix consists of nanometer- to micrometer-sized gaps that may be either open or filled with OM. Their presence enhances access and storage of fluid at these sites. The details of gas accessibility within the core depend, to a great extent, on the geometry and distribution of fractures at all scales, whether open or closed.
- The low-density region at the fracture-fill/rock-fabric interface explains, in part, the weak bond between fracture fill and shale matrix, making the region susceptible to fractures.
- A storage-capacity-enhancing adsorption effect of Kr on calcite and illite was presumed and positively measured. The OM present in the microgaps between the filled fracture wall and shale matrix is most likely susceptible to Kr adsorption, and similarly to methane. The carbonate-rich laminations of the core were found to have consistently greater Kr porosity than the clay-rich laminations that averaged very-low-to-zero porosity in spite of the greater adsorption capability of clays.

Acknowledgments

Portions of this research were carried out at the Stanford Synchrotron Radiation Lightsource, a Directorate of SLAC National Accelerator Laboratory and an Office of Science User Facility operated for the US Department of Energy Office of Science by Stanford University. Other aspects of this work were performed at the Stanford Nanocharacterization Laboratory, part of the Stanford Nano Shared Facilities. The FIB/SEM images were collected by Juliet Jamtgaard with helpful adjustments by Richard Chin. Robert Jones provided technical assistance on electron microprobe analysis and color CL. Electron backscatter diffraction/energy dispersive spectroscopy analysis and processing were performed with Jessica Warren's facility at Stanford University and the SEM facility supported by the Deptartment of Plant Biology at the Carnegie Institution of Washington. The authors give special thanks to Nikolaus Deems for training and assistance. Much of the sample preparation and some of the imaging were conducted at SUMAC SHRIMP RG laboratory, a joint Stanford University-USGS facility. Joe Wooden and Matthew Coble provided helpful suggestions on polishing shale samples. The authors thank Beibei Wang for adsorption measurements made with the Clean Conversions Laboratory of Jennifer Wilcox at Stanford University. Last, the authors wish to thank the technical editors for their insights and valuable suggestions.

References

Akkutlu, Y. and Fathi, E. 2011. Multi-scale Gas Transport in Shales With Local Kerogen Heterogeneities. Presented at the SPE Annual Technical Conference and Exhibition, Denver, Colorado, 30 October–2 November. SPE-146422-MS. http://dx.doi.org/10.2118/146422-MS.

Aljamaan, H. 2013. Petrophysical Investigation on Gas Transport Properties of the Barnett Shale. Presented at the SPE International Student Paper Contest at the SPE Annual Technical Conference and Exhibition, New Orleans, Louisiana, 30 September–2 October. SPE-167624-STU. http://dx.doi.org/10.2118/167624-STU.

Andrews, J.C., Brennan, S., Patty, C. et al. 2008. A High Resolution, Hard X-ray Bio-imaging Facility at SSRL. *Synchrotron Radiation News* **21** (3): 17–26. http://dx.doi.org/10.1080/08940880802123043.

Beebe, R., Beckwith, J.B., and Honig, J.M. 1945. The Determination of Low Surface Areas by Krypton Adsorption at Low Temperatures. *J. Am. Chem. Soc.* **67** (9): 1554–1558. http://dx.doi.org/10.1021/ja01225a048.

Bowker, K.A. 2007. Barnett Shale Gas Production, Fort Worth Basin: Issues and Discussion. *AAPG Bull.* **91** (4): 523–533. http://dx.doi.org/10.1306/06190606018.

Curtis, J.B. 2002. Fractured Shale-Gas Systems. *AAPG Bull.* **86** (11): 1921–1938. http://dx.doi.org/10.1306/61EEDDBE-173E-11D7-8645000102C1865D.

EIA (US Energy Information Administration). 2012. Table 13: Shale Natural Gas Proved Reserves and Production, 2009–12, http://www.eia.gov/naturalgas/crudeoilreserves/pdf/table_13.pdf. (accessed 27 January 2015).

Gale, J.F.W. and Holder, J. 2008. Natural Fractures in the Barnett Shale: Constraints on Spatial Organization and Tensile Strength With Implications for Hydraulic Fracture Treatment in Shale-Gas Reservoirs. Presented at the 42nd US Rock Mechanics Symposium and 2nd US-Canada Rock Mechanics Symposium, San Francisco, California, 29 June–2 July. Paper ARMA-08-096.

Gale, J.F.W. and Holder, J. 2010. Natural Fractures in Some US Shales and Their Importance for Gas Production. The Geological Society, London, Petroleum Geology Conference Series, **7**, pp. 1131–1140. http://dx.doi.org/10.1144/0071131.

Gale, J.F.W., Reed, R.M., and Holder, J. 2007. Natural Fractures in the Barnett Shale and Their Importance for Hydraulic Fracture Treatments. *AAPG Bull.* **91** (4): 603–622. http://dx.doi.org/10.1306/11010606061.

Gasparrini, M., Sassi, W., and Gale, J.F.W. 2014. Natural Sealed Fractures in Mudrocks: A Case Study Tied to Burial History From the Barnett Shale, Fort Worth Basin, Texas, USA. *Marine and Petroleum Geology* **55:** 122–141. http://dx.doi.org/10.1016/j.marpetgeo.2013.12.006.

Gregg, S.J. and Sing, K.S.W. 1982. *Adsorption, Surface Area and Porosity*. Academic Press, second edition, 77–79.

Guo, Z., Chapman, M., and Li, X. 2012. Exploring the Effect of Fractures and Microstructure on Brittleness Index in the Barnett Shale. Presented at the SEG Annual Meeting, Las Vegas, Nevada, 4–9 November. Paper SEG-2012-0771.

Harris, J., Kovscek, A.R., Orr, F.M. et al. 2008. Geologic Storage of Carbon Dioxide. Technical Report of the Global Climate and Energy Project, Stanford University, http://gcep.stanford.edu/research/technical_report/20012.html.

IPCC. 2005. Special Report on Cabon Dioxide Capture and Storage. Chapter 5: Underground Geological Storage, http://www.ipcc-wg3.de/special-reports/special-report-on-carbon-dioxide-capture-and-storage.

Jarvie, D.M., Hill, R.J., Ruble, T.E. et al. 2007. Unconventional Shale-Gas Systems: The Mississippian Barnet Shale of North-Central Texas As One Model for Thermogenic Shale-Gas Assessment. *AAPG Bull.* **91** (4): 475–499. http://dx.doi.org/10.1306/12190606068.

Jessen, K., Tang, G.-Q., and Kovscek, A.R. 2008. Laboratory and Simulation Investigation of Enhanced Coalbed Methane Recovery by Gas Injection. *Transp. Porous Med.* **73** (2): 141–159. http://dx.doi.org/10.1007/s11242-007-9165-9.

Josh, M., Esteban, L., Delle Piane, C. et al. 2012. Laboratory Characterization of Shale Properties. *J. Petrol. Sci. & Eng.* **88–89:** 107–124. http://dx.doi.org/10.1016/j.petrol.2012.01.023.

Katagami, M. 2007. Energy Table for EDS Analysis, http://www.jeolusa.com/DesktopModules/Bring2mind/DMX/Download.aspx?Command=CoreDownload&EntryId=386&Porta1Id=2&TabId=320 (accessed 30 March 2013).

Klington, G.L. and Holmes, J.M. 1953. Adsorption by Evaporated Copper Films at 78°K–Part 1.—Krypton and Hydrogen. *Trans. Faraday Soc.* **49:** 417–425. http://dx.doi.org/10.1039/TF9534900417.

Lash, G.G. and Engelder, T. 2005. An Analysis of Horizontal Microcracking During Catagenesis: Example From the Catskill Delta Complex. *AAPG Bull.* **89** (11): 1433–1449. http://dx.doi.org/10.1306/05250504141.

Laubach, S.E. 2003. Practical Approaches to Identifying Sealed and Open Fractures. *AAPG Bull.* **87** (4): 561–579. http://dx.doi.org/10.1306/11060201106.

Lin, W., Tang, G.-Q., and Kovscek, A.R. 2008. Sorption-Induced Permeability Change of Coal During Gas-Injection Processes. *SPE Res Eval & Eng* **11** (4): 792–802. SPE-109855-PA. http://dx.doi.org/10.2118/109855-PA.

Liu, Y., Andrews, J.C., Wang, J. et al. 2011. Phase Retrieval Using Polychromatic Illumination for Transmission X-Ray Microscopy. *Opt. Express* **19** (2): 540–545. http://dx.doi.org/10.1364/OE.19.000540.

Lockey, K.H. 1960. The Thickness of Some Insect Epicuticular Wax Layers. *J. Exp. Biol.* **37:** 316–329.

Loucks, R.G., Reed, R.M., Ruppel, S.C. et al. 2009. Morphology, Genesis, and Distribution of Nanometer-Scale Pores in Siliceous Mudstones of the Mississippian Barnet Shale. *J. Sedimentary Research* **79:** 848–861. http://dx.doi.org/10.2110/jsr.2009.092.

Loucks, R.G. and Ruppel, S.C. 2007. Depositional Setting and Lithofacies of the Mississippian Deepwater Barnett Shale in the Fort Worth Basin, Texas. *AAPG Bull.* **91:** 579–602.

Montgomery, S.L., Jarvie, D.M., Bowker, K.A. et al. 2005. Mississippian Barnett Shale, Fort Worth Basin, North-Central Texas: Gas-Shale Play With Multi-Trillion Cubic Foot Potential. *AAPG Bull.* **89** (2): 155–175.

Nuttall, B., Drahovzal, J., Eble, C. et al. 2005. CO_2 Sequestration in Gas Shales of Kentucky. Oral presentation at the AAPG Annual Convention, Calgary, Alberta, Canada, 19–22 June.

Ottinger, S., Pini, R., Storti, G. et al. 2006. Adsoprtion of Pure Carbon Dioxide and Methane on Dry Coal From the Sulcis Coal (SW Sardinia, Italy). *Environ. Progress* **25** (4): 355–364.

Papazis, P.K. 2005. *Petrographic Characterization of the Barnett Shale, Fort Worth Basin, Texas*. MS thesis, University of Texas, Austin (August 2005), 142 p.

Passey, Q.R., Bohacs, K.M., Esch, W.L. et al. 2010. From Oil-Prone Source Rock to Gas-Producing Shale Reservoir–Geologic and Petrophysical Characterization of Unconventional Shale-Gas Reservoirs. Presented at the CPS/SPE International Oil and Gas Conference and Exhibition, Beijing, China, 8–10 June. SPE-131350-MS. http://dx.doi.org/10.2118/131350-MS.

Reed, R.M. and Milliken, K.L. 2003. How to Overcome Imaging Problems Associated With Carbonate Minerals on SEM-Based Cathodoluminescence Systems. *J. Sedimentary Research* **73** (2): 328–332. http://dx.doi.org/10.1306/081002730328.

Roberts, M.W. 1960. The Interaction of Krypton, Oxygen and Hydrogen With Iron Films. *Trans. Faraday Soc.* **56:** 128–137. http://dx.doi.org/10.1039/TF9605600128.

Ross, D.J.K. and Bustin, R.M. 2008. Characterizing the Shale Gas Resource Potential of Devonian-Mississippian Strata in the Western Canada Sedimentary Basin: Application of an Integrated Formation Evaluation. *AAPG Bull.* **92** (1): 87–125. http://dx.do.org/10.1306/09040707048.

Ross, D.J.K. and Bustin, R.M. 2009. The Importance of Shale Composition and Pore Structure Upon Gas Storage Potential of Gas Shale Reservoirs. *Marine and Petroleum Geology* **26** (6): 916–927. http://dx.doi.org/10.1016/j.marpetgeo.2008.06.004.

Tran, D.T., Roegiers, J.-C., and Thiercelin, M. 2010. Thermally-Induced Tensile Fractures in Barnett Shale and Their Implications to Gas Shale Fracability. Presented at the 44th US Rock Mechanics Symposium and 5th US-Canada Rock Mechanics Symposium, Salt Lake City, Utah, 27–30 June, 14 p. Paper ARMA-10-466.

USGS National Assessment of Oil and Gas Resources Team, and Biewick, L.R.H., compiler. 2013. Map of Assessed Shale Gas in the United States, 2012: US Geological Survey Digital Data Series 69–Z, 16 p., 1 pl.

Vega, B., Andrews, J.C., Liu, Y. et al. 2013. Nanoscale Visualization of Gas Shale Pore and Textural Features. Presented at the Unconventional Resources Technology Conference, Denver, Colorado, 12–14 August. SPE-1581981-MS. http://dx.doi.org/10.2118/1581981-MS.

Vega, B., Dutta, A., and Kovscek, A.R. 2014. CT Imaging of Low-Permeability, Dual-Porosity Systems Using High X-ray Contrast Gas. *Transp. Porous Med.* **101:** 81–97. http://dx.doi.org/10.1007/s11242-013-0232-0.

Wang, B. 2014. *The Role of Kerogen Versus Clay in the Adsorption Mechanisms of CO_2 in Gas Shales*, MS Thesis, Department of Energy Resources Engineering, Stanford University, Stanford, California (June 2014).

Wong, S., Gunter, W.D., and Mavor, M.J. 2000. Economics of CO_2 Sequestration in Coalbed Methane Reservoirs. Presented at the 2000 SPE/CERI Gas Technology Symposium, Calgary, Alberta Canada, 3–5 April. SPE-59785-MS. http://dx.doi.org/10.2118/59785-MS.

Bolivia Vega is a research associate in the Department of Energy Resources Engineering at Stanford University, where she has worked for more than 7 years. Her current research interests are low-permeability porous-media fluid-transport mechanisms and enhanced oil recovery (EOR), as well as multiscale imaging of static and dynamic fluid-flow systems. Vega is an SPE member and has served as section chair for the SPE Golden Gate Section and currently is a Section and Chapter Activities Committee member. She holds an MS degree in petroleum engineering from Stanford University and a BS degree in chemical engineering from Simon Bolivar University, Venezuela.

Cynthia M. Ross is a research associate in the Department of Energy Resources Engineering at Stanford University. She has coauthored numerous technical papers and holds a US patent. Ross' current projects involve characterization of reservoir diatomites and shales. She holds MS and PhD degrees in geology from the University of South Carolina. Ross is a member of SPE, the Society of Professional Well Log Analysts, and the American Association of Petroleum Geologists.

Tony Kovscek is a professor and chair of the Department of Energy Resources Engineering at Stanford University. His research interests center around the recovery of unconventional hydrocarbons. Kovscek holds BS and PhD degrees from the University of Washington and the University of California, Berkeley, respectively.